Lawrence Berkeley National Laboratory
LBL Publications

Title

Zeolitization of a devitrified high-silica rhyolitic tuff producing dachiardite: A comparison of hydrothermal experiments with the corresponding reaction progress modeling

Permalink

https://escholarship.org/uc/item/95t6b44x

Authors

Knauss, Kevin G
Saldi, Giuseppe D
Spycher, Nicolas F

Publication Date

2023-08-01

DOI

10.1016/j.apgeochem.2023.105741

Copyright Information

Peer reviewed

Zeolitization of a devitrified high-silica rhyolitic tuff producing dachiardite: A comparison of hydrothermal experiments with the corresponding reaction progress modeling

Kevin G. Knauss [a],[*], Giuseppe D. Saldi [b], Nicolas F. Spycher [a]

[a] *Energy Geosciences Division, Lawrence Berkeley National Laboratory, 1 Cyclotron Road, Berkeley, CA, 94720, USA*
[b] *Physics and Geology Department, University of Perugia, Piazza dell'Università, 1, 06123, Perugia PG, Italy*

ARTICLE INFO

ABSTRACT

We have investigated the hydrothermal alteration of polished wafers of tuff reacted with dilute groundwater at 90 °C, 150 °C and 250 °C for time periods ranging from 2 months to nearly 1 year. The polished rock wafer provided a convenient surface upon which to grow secondary minerals. Reaction product minerals were identified and analyzed at the end of each experiment and, along with the evolving fluid chemistry, were compared to computational results from corresponding reaction progress models.

At 250 °C after a few months the run products in the experiment were dominantly the mordenite group zeolite minerals: dachiardite (a Ca-rich variety) and mordenite, itself. At 150 °C after a few months of reaction only minor amounts of clay were produced, but after 1 year of reaction at this temperature both mordenite group zeolites were again present. At this lower temperature the total amount of run products was much smaller. At 90 °C no run products could be seen at all, even after 1 year of reaction. The reaction progress modeling results for reaction products were in good relative agreement with the experimental results.

The higher the temperature, and the greater the extent of reaction, the better the fluid phase modeling results agreed with the actual experimental results. At 250 °C the agreement was good for nearly all elements. At 150 °C agreement for pH, SiO_2, Na and K were good, but less good for Al, Mg and Ca, especially after short reaction times. At 90 °C agreement for pH, SiO_2 and Na was reasonable, but not as good for the other elements, and all modeling results for short reaction times did not match experimental results as well as the longer time results.

This study demonstrates that reaction progress modeling provides a powerful tool for predicting hydrothermal rock-water interactions, with results expected to improve, as more and better quality thermodynamic and kinetic data become available and as process-oriented simulators incorporate better and more comprehensive sub-models for mineral dissolution and growth.

1. Introduction

The Yucca Mountain Project was created in 1987 to study the suitability of storing nuclear waste in an underground repository in Nevada sited within the Topopah Spring Member of the Paintbrush Tuff (Tpt), a densely welded, rhyolitic tuff. Following extensive geologic, hydrologic, and geochemical studies, in 2002 it was officially designated as the site for the repository to store the nation's spent fuel and high-level radioactive waste. In 2011 funding was terminated and no replacement site has yet been identified (Rutqvist and Tsang, 2012).

Some of the geochemical studies undertaken in this project were designed to investigate rock-water interactions that could occur during the thermal period following waste emplacement. These studies involved detailed measurements of both the fluid and solid phases undergoing hydrothermal alteration, as well as the reaction product minerals. The results (Knauss et al., 1985b, 1987) comprise a body of experimental data well suited for evaluating the ability of current reaction progress models (and widely used thermodynamic and kinetic data) to "predict" these interactions, specifically without the usual "fitting" exercise to improve agreement.

For this purpose, we selected a subset of the experiments that reacted solid polished wafers of this rock with a natural groundwater (a dilute Na–HCO₃ composition) largely produced from this same Tpt geologic unit. Additional experiments were conducted using deionized water to

---

* Corresponding author.
  E-mail address: kgknauss@lbl.gov (K.G. Knauss).

confirm that under these relatively high water/rock ratios, the dilute natural water produces similar fluid chemistry evolution to that produced by deionized water. Under these conditions the rock composition is the controlling factor in determining the evolving fluid composition. The experiments spanned a range in temperature and time, permitting evaluation of overall appropriateness of the utilized models and, indirectly, the thermodynamic and kinetic data input into these models.

The specific purposes of this study were: 1) to evaluate the fluid chemistry evolution and the production of secondary minerals that result from hydrothermal reaction of a dilute bicarbonate groundwater with a crystalline (devitrified) high silica rhyolitic tuff and 2) to make a preliminary evaluation of the ability of the popular reactive transport model TOUGHREACT (Xu et al., 2006, 2011) and the current Thermoddem thermodynamic database (Blanc et al., 2012), when used in conjunction with a common source of mineral kinetic data (Palandri and Kharaka, 2004), to accurately simulate this interaction. Simulation of the evolution of the composition of both the rock and the water as they react can be compared directly to corresponding experimental results.

We present here the results of this comparison and a discussion of the limitations of the model in reproducing the experimental data.

2. Methods

2.1. Starting materials

The reacting fluid used in the 5 reported experiments (DB8, 9, 12, 13 and 14) was a natural groundwater from well J13. This well was drilled by the USGS in 1963 and is located in the southwest corner of Jackass Flats in Forty-Mile Wash on the Nevada Test Site. It produces largely from a highly fractured interval within the Tpt formation at a depth of 728 m. Two additional experiments (DB16 and 17) used deionized water. The exact composition of the J13 water used was measured at the start of each experiment, and the average composition is shown in Appendix Table A1. This composition compares well with earlier compilations (Delany, 1985).

The tuff being reacted was from the Topopah Spring Member of the Paintbrush Tuff (Tpt). This unit is part of the Timber Mountain-Oasis Valley caldera complex that lies within a volcanic field in southern Nevada, which once covered 11,000 km². The caldera complex, active from 16 to 9.5 Myr. ago, was the source of nine voluminous rhyolitic ash-flow sheets and numerous smaller rhyolitic tuffs and lava flows (Christiansen et al., 1977). At the collected sample depth the rock is a densely welded, vapor-phase-altered, and crystal-poor high-silica rhyolite (Bish et al., 1981). Based on many XRD analyses the devitrified groundmass mineralogy within this part of the unit consists (in order of abundance) of: cristobalite (30–50%), alkali feldspar (30–50%) and quartz (10–20%), all present as micron (or slightly larger) sized crystals. The exact mineralogic composition of the reacted samples is presented in the Results section. Authigenic recrystallization produced quartz and alkali feldspar within relict pumice. Phenocrysts in the Topopah Spring Member are scarce (0–2%). The predominant phenocryst phases present are plagioclase (An16), alkali feldspar (Or57), and Fe–Ti oxides. Rarely, embayed quartz and biotite are present. Altered pyroxene and biotite phenocrysts are present in trace amounts.

Based on the quantitative electron microprobe (EMP using WDS – wavelength dispersive x-ray spectrometry) analyses of multiple points on a polished thin section prepared from the sub-core used to prepare the wafers described below, we determined the specific composition of the unreacted tuff. The devitrified groundmass that comprised the bulk

(≥98%) of the rock had the composition shown in Table 1.

The starting solid in each experiment was a polished wafer of tuff. We prepared the wafers by subsampling (using a 1 in. diameter corer) the center of NX-size (~3 in. diameter) drillcore from well USW-G1 (Bish et al., 1981) at a depth of 1232 ft. A small hole (~0.1 in. diameter) was then drilled through the center of the resulting 1 in. diameter subcore. The subcore was sliced into 0.1 in. thick wafers. The wafers averaged 2.30 (±0.04) g in weight. In the model for each individual experiment the exact weight of that wafer was used. Mercury porosimetry and Ar BET surface area measurements made on an unreacted core wafer (prepared identically to those used in the experiments) yielded a surface area of 0.378 m^2/g, a bulk density (ρ_b) = 2.36 g/cm³, and a grain density (ρ_g) = 2.52 g/cm³ (Delany, 1985).

Both coring and slicing used a mixture of water and water-soluble oil as lubricant. Both sides of each wafer were then rough ground using 10 μm aluminum oxide and polished optically flat using 1 μm and then finally 0.3 μm aluminum oxide. The polished wafers were then washed repeatedly in distilled water and cleaned ultrasonically to remove any adhering aluminum oxide and fine particles possibly created in cutting and polishing. This was confirmed using scanning electron microscopy (SEM) imaging.

2.2. Experimental setup

Experiments were conducted at constant pressure and temperature in flexible gold reaction systems sealed with an acid-cleaned and passivated (oxidized) titanium head (Seyfried et al., 1979). The gold-+titanium reactor is suspended within an alloy pressure vessel that uses distilled water as the pressuring medium. The pressure vessel is located within a large tube furnace that can be rocked continuously through a 180° arc, and then stopped periodically for sampling. Experimental conditions were always a single aqueous liquid phase with no headspace gas phase, facilitated by the very flexible Au bag. The Au bag reactors are nominally 220 mL in volume, but the exact starting fluid volume varied from 179 to 222 mL, depending on the specific temperature and pressure of a given experiment. These reactors allow the aqueous fluid and dissolved gas in each experiment to be sampled multiple times over the course of an experiment at nearly constant pressure and temperature. A passivated sintered Ti frit (nominally 10 μm) located on the inside of the Ti head serves as an initial filter for the fluid exiting the Au bag through an acid-cleaned and passivated capillary Ti exit tube. A schematic of the experimental apparatus is shown in Appendix Fig. A1.

The Ti head/closure was modified to suspend the solid polished wafers, holding them motionless relative to the rocking reaction cell. The Ti gland nut that holds the sintered Ti frit is threaded to accept a small Ti bolt. The polished wafer with a small central drilled hole is sandwiched between two washers cut from gold mesh and held in place by the Ti bolt. In this way the wafer is exposed to fluid on both sides and edges and affords a convenient surface upon which secondary minerals may grow as a result of hydrothermal rock-water interaction.

2.3. Experimental Sampling and analyses

The fluid exiting the sampling tube through a Ti high pressure valve is delivered into a gas-tight syringe. Following a bleed to remove stagnant solution from the small volume exit tube, several samples are withdrawn: an unfiltered sample for immediate pH measurement, another unfiltered sample for immediate infrared (IR) CO_2 analyses, and then two filtered samples using an inline filter (0.1 μm) between the Ti

Table 1
EMP analyses of the groundmass.

Wt%	SiO₂	Al₂O₃	FeO	MgO	CaO	Na₂O	K₂O	TiO₂	MnO	total
Mean	70.69	11.32	0.49	0.01	0.32	3.51	5.09	0.08	0.05	100.55
SD	2.13	0.74	0.12	0.01	0.07	0.25	0.50	0.03	0.02	2.33

valve and the syringe. The first filtered sample is delivered into a pre-acidified glass gas-tight syringe for cation analyses (by ICP-ES and AA-S for Al, Si, Ca, K, Mg, Na, Fe, Mn), and the second is unacidified for anion analyses (by IC and IR-CO_2 for F, Cl, NO_3, SO_4 and HCO_3). Note that although Fe and Mn were analyzed in all samples, because the experiments were initially air-saturated, the oxidized conditions rendered their concentrations at or near detection limits in most samples and are not reported here. The total fluid volume removed during a sampling session is approximately 13 mL.

At the termination of each run the furnaces were switched off, followed by several hours of cooling, until the vessels could be disassembled. The solid wafers were recovered, rinsed gently in MQ water, and then air dried in a desiccator to constant weight.

The entire wafer surface was examined at high magnification using SEM in back-scattered electron image mode (BEI) to locate run products. In most experiments the secondary minerals found were characterized compositionally using semi-quantitative energy dispersive x-ray spectroscopy (EDS) only. The EDS spectra were plotted and a semi-quantitative analysis was done. Morphology, crystal habit and EDS composition were used to make tentative identification. However, in the 250 °C experiment (DB9) one of the zeolite minerals formed (the mordenite group minerals: dachiardite and mordenite) was so large (the dachiardite was up to 70 μm long) that it could be easily removed by handpicking under a binocular microscope. This mineral was positively identified using XRD and a Gandolfi camera to yield precise cell dimensions. A polished grain mount of the plucked dachiardite crystals was prepared for WDS analyses and 45 quantitative results (alkali-aluminum balance E $<\pm 7\%$ (Passaglia, 1970);) were obtained. The resulting chemical formula for this dachiardite is shown below in the Results section.

In Table 2 we show the specific experimental conditions for each experiment. Note that during each experiment pressure was maintained at the average values shown, varying by ± 5 bar or less only during sampling. In every case the pressure was always significantly above the water vapor pressure (P_{sat}) for the experimental temperature, assuring that the system remained a single aqueous phase with no headspace gas. In these silicate/oxide mineral-water systems at relatively low temperatures and pressures, mineral solubilities and reaction kinetics are essentially pressure independent. In the subsequent modeling we assumed a consistent 50 bar pressure for the reaction progress simulation.

2.4. Reaction progress simulation approach

The conceptual model for the flexible gold reaction system is a Static Batch Reactor comprised of a single (numerical) cell. The fluid volume in each experiment varies, depending on the temperature and pressure conditions of the run, and in each case the simulation matches that of the corresponding physical experiment.

In this model at time t = 0 the Au Bag Reactor is filled with the desired amount of the reacting fluid (either J13 water or MQ water) and contains the Tpt wafer to be reacted. Following initial 20 °C speciation computations with the fluid at t = 0, the model fluid temperature is instantaneously raised to the temperature of the corresponding

experiment (90°-250 °C), speciation re-computed, followed by the simulation of kinetically controlled chemical reaction with the solid. The pressure in the simulation is set to a constant value of 50 bar. We simulated the closed system experiments as closely as possible, including fluid sample withdrawals. The models simulate nearly instantaneous (~20 s) extraction of fluid mass equal to the physical sample mass, and then proceed with the simulation using reduced volume, mass, and liquid-solid ratio, thereby accounting for the removed fluid and any of the mineral components that may have dissolved in it.

To simulate the reaction of Tpt rock with J13 dilute groundwater, the conceptual model described above was implemented numerically with the TOUGHREACT (TR) reactive transport simulator (Xu et al., 2006, 2011) (in-house upgrade of version 3.32), together with its equation of state module EOS1.

The thermodynamic data used for the modeling was from the Thermoddem database (Blanc et al., 2012), and specifically from the latest datafile: ToughReact_ThermoddemV1.10_15Dec2020. dat. This database uses the aqueous species NH_3 as the primary species for the element N. Because the experiments were conducted under relatively oxidizing conditions where NH_3 would be in very low abundance and NO_3^- would be the dominant species, in order to avoid potential convergence issues, the NO_3^- primary species was swapped for NH_3, and equilibrium constants (log K values) for all N-containing reactions in the database were recalculated, accordingly.

In the simulations, when appropriate, the ideal mixing solid solution model implemented in TOUGHREACT was used. A binary solid solution, plagioclase-ss (endmembers albite and anorthite), was assumed for the thermodynamic properties of the reacting plagioclase feldspar component of the devitrified groundmass. We used a solid solution, montmorillonite-ss, as representative of the secondary clay minerals formed as a result of rock-water interaction and allowed it to precipitate as a quaternary solid solution between Ca, K, Mg and Na end-members (Aradottir et al., 2012).

The dominant reaction product in some of the experiments was dachiardite; unfortunately, not much data are available concerning either the thermodynamics or kinetics of dachiardite formation or its dissociation. Calorimetric measurement of the enthalpy of formation of dachiardite from the constituent oxides and elements was first reported by Ogorodova et al. (2007). These authors estimated the Gibbs energy of formation of the zeolite and other thermodynamic properties using a variety of approaches. More recently, a very comprehensive compilation of zeolite thermodynamic data for assessing zeolite stability during the corrosion of nuclear waste immobilization glasses has become available (Bi et al., 2020), although this database is limited to low temperature (<95 °C) and pressure (1 bar). However, kinetic data are still lacking. Hence, for consistency with the Thermoddem database, we elected to simply use the Ca-end member mordenite composition (MordeniteB (Ca)) that is present in that database, and the kinetic data for laumontite dissolution kinetics (Savage et al., 1993) as proxies for the missing dachiardite quantities. More details are in the Simulation Results section 3.2.

Rate laws derived from Transition State Theory - TST (Lasaga, 1984) were used in the simulations with the reaction rate R defined as:

$$R = SA \bullet k \bullet (1-(Q/K)^n)$$

With SA being the mineral surface area, k being the surface area normalized rate constant, Q/K representing the mineral saturation ratio (ion activity product Q divided by the equilibrium constant K), and n being an exponent related to the Temkin coefficient (e.g., Lichtner, 2016) that is a function of the mineral formula unit (here taken as the inverse of the number of Si atoms in the mineral formula for silicates, and unity for other minerals). The rate constant k was implemented with multiple mechanisms (acid, neutral and alkaline pH ranges) as described in Xu et al. (2006) and Palandri and Kharaka (2004) as follows:

Table 2
Experimental conditions and run duration for each experiment.

Experiment	T (°C)	Ave. P (bar)	Duration (days)	Fluid
DB14	90	62	49	J13
DB12	90	25	302	J13
DB8	150	69	66	J13
DB13	150	45	302	J13
DB9	250	62	66	J13
DB17	90	62	64	MQ[a]
DB16	150	83	64	MQ[a]

[a] = Milli-Q, 18MΩ•cm deionized water.

$$k = k_{25}^{nu} \, exp\left[\frac{-E_a^{nu}}{R}\left(\frac{1}{T} - \frac{1}{298.15}\right)\right] + k_{25}^{H} \, exp\left[\frac{-E_a^{H}}{R}\left(\frac{1}{T} - \frac{1}{298.15}\right)\right] a_H^{n_H}$$

$$+ k_{25}^{OH} \, exp\left[\frac{-E_a^{OH}}{R}\left(\frac{1}{T} - \frac{1}{298.15}\right)\right] a_{OH}^{n_{OH}}$$

where: k is the rate constant (mole m^{-2} s^{-1}); E_a is the activation energy (J mole^{-1}); R is the Gas Constant (J K^{-1} mole^{-1}); T is the temperature of interest (K); superscripts or subscripts nu, H, and OH indicate neutral, acid and base mechanisms, respectively; a is the activity of the sub-scripted species; and n is a power term (constant). This 3-term equation accounts for separate mechanisms for each pH region (acid, neutral and basic). It has been shown that for some minerals, depending on the co-ordination state of Al and the pH, rates can also depend on Al^{3+} activity (Oelkers et al., 1994, 2008; Oelkers and Gislason, 2001). Following the approach of Marieni et al. (2021) we have used the more pragmatic rate constant equation shown above based only on proton activity for our simulations.

The kinetic rate law data used in the simulations are provided in Table 3. For consistency these are taken directly from Palandri and Kharaka (2004) without further modification with the exception of laumontite (Savage et al., 1993), which is not contained in the Palandri and Kharaka compilation. Indeed, no zeolites are contained in their compilation. Note that the rate data for the plagioclase-ss correspond to that of albite, which is appropriate given the measured composition of the devitrified groundmass and the calculated end member feldspar compositions (Blum and Stillings, 1995; Knauss et al., 1985a, b, 1987). The variability in experimentally measured mineral dissolution (and precipitation) rate constants can vary from mineral to mineral and the reader is directed to Sec. 2.3 of Palandri and Kharaka (2004) for an evaluation of the limitations and uncertainties of their compilation. Note that for those minerals in the simulation that are permitted to grow, the rate law is simply run in reverse, i.e., the dissolution and precipitation rate constants, activation energy and reaction order are the same. Although TOUGHREACT can accommodate a degree of supersaturation required prior to mineral growth, we did not invoke this option (except for one example provided in the Appendix – see the Discussion section for details). Because the actual secondary mineral growth was only determined at the end of each experiment, quantifying a possible su-persaturation effect was not feasible.

The selection of potential secondary minerals in the model was informed by initial speciation-solubility calculations made using the measured experimental sample solution compositions and, later, by direct observation and positive identification in the post-test SEM, EMP and XRD (Gandolfi camera) analyses of the reacted wafers recovered from each experiment. The suite of minerals likely to form can differ as a function of temperature, so for consistency in each model we included all the phases that were possible at any of the temperatures. Based on the thermodynamic and kinetic processes at play, the code would determine which of them would be appropriate as each model system evolved. This topic will be dealt with in greater detail in the following Results section.

3. Results

3.1. Experimental results

The fluid compositional data for each experiment are contained in Appendix Tables A2 – A8. All data are blank- and dilution-corrected. They are compared directly to the corresponding simulation results in subsequent plots in section 3.2.1 and in the Appendix. Although we present the results of the deionized water experiments in Tables A7 and A8 to compare to the equivalent dilute groundwater experiments, plots of those results are not shown.

At the conclusion of each experiment the recovered wafers were examined by SEM, looking for reaction products. Identifiable run products were found on wafers from experiments DB8 (150 °C, 66 days), DB13 (150 °C, 302 days) and DB9 (250 °C, 66 days). We only discuss the fluid and solid phase results for those experiments in which identifiable run products were found. The results for the two 90 °C experiments, in which no identifiable run products were found, are presented in the Appendix.

In the short-term 250 °C experiment (DB9) the effects of the hy-drothermal interaction of groundwater and tuff were readily apparent. After 66 days of reaction the wafer had a 5.7% weight loss. The disso-lution effects on phenocrysts (present at ~2%) were seen as highlighting of twinning in plagioclase feldspars by the formation of etch pits, pre-sumably along the more anorthitic lamellae, and the general corrosion of biotite. The very much smaller (micron to sub-micron) alkali feldspar and cristobalite crystals formed by the granophyric devitrification of the originally glassy tuff matrix and by vapor phase deposition in lith-ophysal cavities were particularly prone to attack.

Based on crystal habit, morphology, and EDS semi-quantitative chemical analyses, on the 250 °C reacted wafer we infer the presence of relatively abundant sheaves of mordenite (high confidence, Fig. 1a - arrow), a minor amount of a poorly crystalline K-bearing claylike phase seen growing on top of dachiardite and over the corroded groundmass (lower confidence, Fig. 1b - arrow) and a rare, perfectly spherical, pure silicon phase likely to be cristobalite.

By far the most abundant secondary mineral produced was the mordenite-group zeolite: dachiardite (Bargar et al., 1987; Bargar and Beeson, 1981; Bonardi, 1979). It occurred as abundant, large prismatic crystals with smaller interpenetrating crystals (Fig. 1c) and rosettes of crystals (Fig. 1a, d). The smaller, interpenetrating crystals grew at a

Table 3
Kinetic data used in the generalized rate equation.

Mineral	Acid Mechanism			Neutral Mechanism		Base Mechanism		
	log k[a]	E[b]	n	log k	E	log k	E	n
Quartz	–	–	–	−13.34	90.1	–	–	–
Cristobalite	–	–	–	−12.31	65.0	–	–	–
Plagioclase-ss	−10.16	65.0	0.457	−12.56	69.8	−15.6	71.0	−0.572
Microcline	−10.06	51.7	0.500	−12.41	38.0	−21.20	94.1	−0.823
Montmorillonite-ss[c]	−12.71	48.0	0.220	−14.41	48.0	−14.41	48.0	−0.130
Kaolinite	−11.31	65.9	0.777	−13.18	22.2	−17.05	17.9	−0.472
MorderiteB(Ca)[d]	–	–	–	−12.25	58.0	–	–	–
MorderiteJ[d]	–	–	–	−12.25	58.0	–	–	–
Calcite	−0.30	14.4	1	−5.81	23.5	−3.48	35.4	1[e]
Magnesite	−6.38	14.4	1	−9.34	23.5	−3.22	62.8	1[e]

a = rate constant in mole m^{-2} s^{-1}.
b = activation energy in kJ mole^{-1}.
c = assume equal to the Montmorillonite-K in Palandri and Kharaka (2004).
d = assume equal to Laumontite in Savage and Cave (Savage et al., 1993).
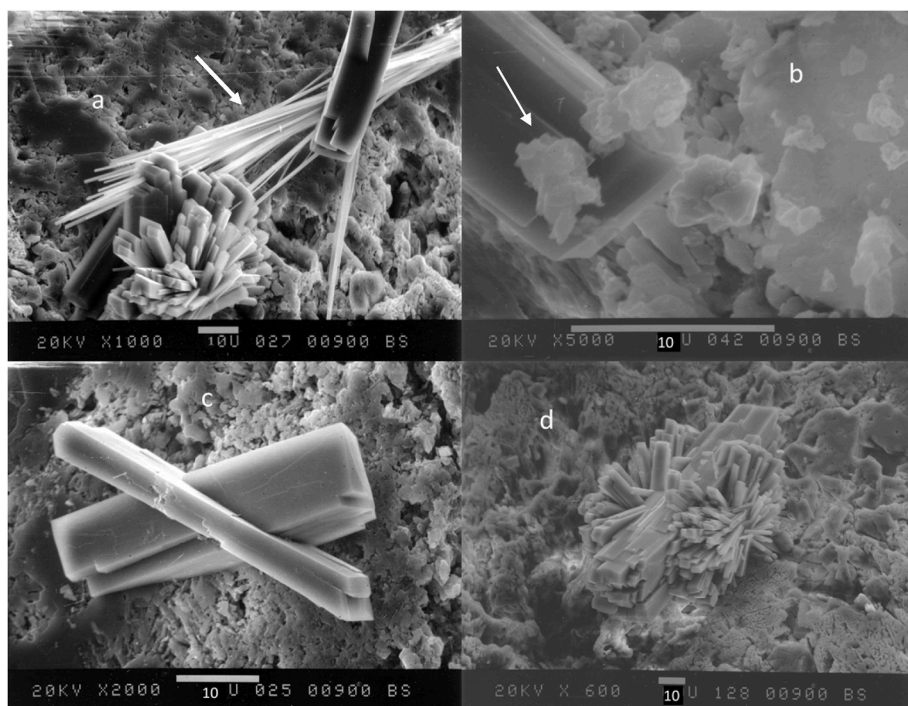e = reaction order with respect to CO_3^{2-} as the catalyzing species, not OH^{-}

Fig. 1. a) on the wafer from experiment DB9 (250°C-short term) the two mordenite-group zeolites (dachiardite and mordenite with arrow) were clearly growing simultaneously, b) clay platelets with arrow on dachiardite crystal and corroded groundmass, c) intergrown, prismatic dachiardite crystals with smaller, interpenetrant crystals growing at preferred angles and d) rosettes of many dachiardite crystals, some of which displayed re-entrant angles suggesting polysynthetic twinning, while some dachiardite crystal masses displayed both forms. Scale bars are all 10 μm in length.

preferred angle from the dominant faces (010) and (100). The prismatic dachiardite was well-terminated, usually by (001), (−101) and (−403). The two mordenite-group zeolites (dachiardite and mordenite) were clearly contemporaneous (Fig. 1a).

The Ca-rich dachiardite and the mordenite produced in this experiment appeared to have grown at the elevated temperature of the run, rather than during the vessel quench at the end of the run. Although not reported in the fluid data tables or figures, the composition of the quench fluid was determined following many experiments. These fluids, which were quenched from the elevated T of the experiment to near room T while remaining in contact with the solid (usually over the course of several hours overnight as the vessel was cooled), all showed the same trends in composition. Invariably, K, Al and pH decreased slightly, while Ca and Mg increased. The Si and Na concentrations appeared to remain stable. However, a decrease in Si that would be appropriate for the minor formation of a K–Al-clay as a quench product would hardly be noticeable. These changes in the fluid composition during the quench from 250 °C suggest that the minor amount of the small clay-like phases (e.g., Fig. 1b) could possibly be a product of the quench. The dachiardite and mordenite, in contrast, are Ca-rich, large, and relatively abundant; hence, the change in fluid composition during the relatively quick quench could not have produced them. This topic (possible quench products) will be dealt with in more detail in the Discussion section.

Because the dachiardite was so common and occurred in such large clusters of crystals, it was thoroughly characterized by hand-picking from the surface of the wafer once the experiment was completed. The dachiardite was positively identified based on its XRD pattern produced in a single crystal Gandolfi x-ray camera. By this method some 26 lines were matched with those contained on JCPDS Card 18–467 for Elba dachiardite. The measured d-spacings of lines were used in a linear regression technique to calculate cell constants (Sheldrick, 2008). The refined cell constants were:
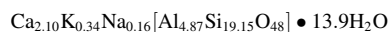
$a_o = 18.645$ Å

$b_o = 7.483$ Å

$c_o = 10.247$ Å

$V_o = 1358$ Å^3

$\beta_o = 108°09'$

A polished grain mount of dachiardite crystals was analyzed by quantitative WDS. On the basis of 45 analyses (all with alkali-aluminum balance (E) $<\pm7\%$ (Passaglia, 1970),) with water calculated by difference, the composition was determined to be:

$Ca_{2.10}K_{0.34}Na_{0.16}[Al_{4.87}Si_{19.15}O_{48}] \bullet 13.9H_2O$

and the calculated density was 2.18 g/cm^3. This compares favorably with the measured density of the type locality Elba dachiardite of 2.17 g/cm^3 (Nishido and Otsuka, 1981). The waters of hydration reported in the literature range from 12.4 to 14.2 for Na-rich dachiardite, while the Elba (Ca-rich) dachiardite contained 12.7 waters, in good agreement with the measured 13.9 waters in the composition above (Alberti, 1975; Bonardi, 1979; Bonardi et al., 1981; Gellens et al., 1982; Wise and Tschernik, 1978). There was an inverse relation between Si/Al and Ca, and possibly a weak direct relation of Si/Al and K, which suggests some degree of substitution of Na + K + Si for Ca + Al. Step-scan WDS analyses every 2 μm across and along dachiardite grains showed no evidence of zoning for Na, K or Ca. The composition of the dachiardite crystals and the relative proportions of the cations remained constant despite a fluid phase whose composition evolved with time of reaction.

In the short term 150 °C experiment (DB8) the effects of hydrothermal reaction were much less severe. The net weight loss was 1.8% of the initial wafer weight. The secondary minerals that were seen were less developed, less crystalline, and far less abundant than at 250 °C. The identity of the run products could only be inferred from semi-quantitative analyses of the EDS spectra and morphology. Based on their semi-quantitative composition, they are thought to include: K-, Ca-, Mg- and/or Fe-bearing claylike phases, gibbsite (or boehmite) and cristobalite. An example of each of these phases grown in experiment DB8 is shown in Fig. 2a, b, and 2c.

In the long-term experiment at 150 °C (DB13) the visible effects of hydrothermal interaction on primary phases were not nearly as severe as at 250 °C which had a 5-fold shorter reaction time. The net wafer weight
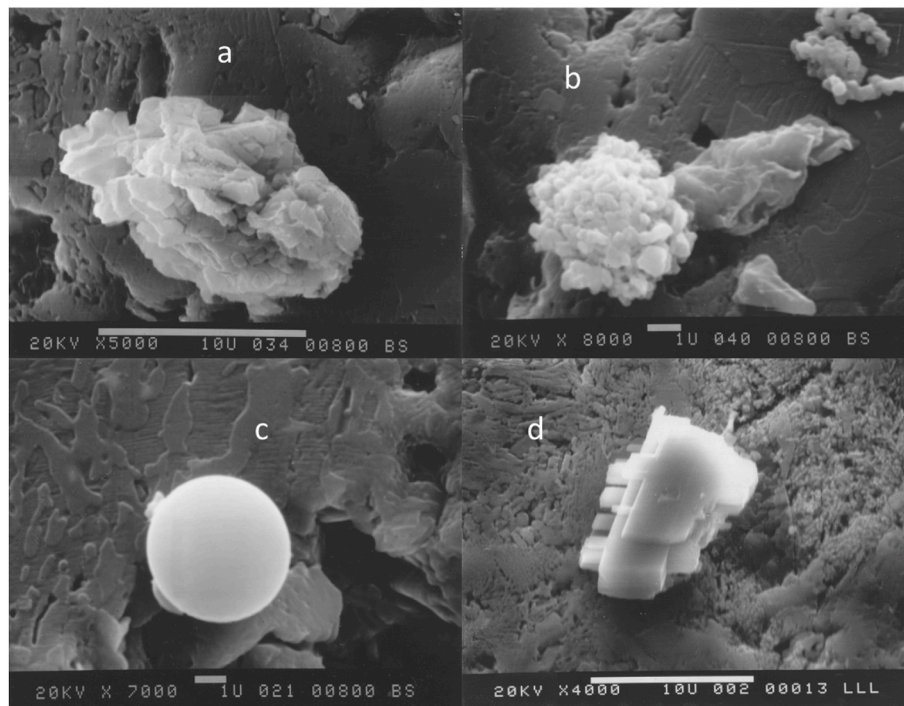
Fig. 2. a) K-bearing clay-like phase, b) pure Al phase (probably boehmite), c) a rare pure Si phase tentatively identified as cristobalite found on the wafer recovered from experiment DB8 (150°C-short term) and d) prismatic forms of dachiardite formed during experiment DB13 (150°C–long term). Scale bars in Fig. 2a and d are 10 μm in length, while those in Fig. 2b and c are 1 μm in length.

loss was again 1.8%, like the shorter experiment at this same temperature (DB8). Interestingly, the wafer surface was largely devoid of the poorly crystalline material (clays, etc.) found on the DB8 wafer. Instead, there were a small number of well-developed, well-crystallized minerals that looked identical (but much smaller) to the dachiardite formed in the 250° experiment (Fig. 2d). The semi-quantitative EDS compositional data of the presumed dachiardite were very similar to the comparable EDS compositions determined in the 250 °C experiment (DB9), where the dachiardite was positively identified and where quantitative WDS analyses were obtained.

In the short-term experiment at 90 °C (DB14) the wafer weight loss was 0.1%, while the 5 times longer reaction at this temperature (DB12) resulted in 0.17% weight loss. No run products of any kind were found on the surfaces of either wafer. The phenocrysts showed little evidence of reaction (no etch pits highlighting twinning lamellae, etc.) and the groundmass minerals looked nearly identical to the unreacted (similarly prepared) wafer that was used as a control.

3.2. Simulation results

As alluded to in the Methods section 2.4, we set up each simulation to match exactly the corresponding physical experiment. We used the J13-average water composition reported in Appendix Table A1 as the starting fluid and the starting mineralogy is that shown in Table 4. The idealized mineral abundances in this table are similar to those determined from XRD and EMP analyses (Sec. 2.1).

The estimated specific surface area for each mineral initially present in the simulation was calculated using the approach suggested by Testor et al. (1994). The geometric specific surface area (SSA) of each mineral is calculated assuming the grains are smooth spheres with surface areas and mass based on an effective spherical diameter (d_e) and density (ρ):

$$\text{Geometric SSA} = \pi (d_e)^2 / (\pi/6)\,(d_e)^3 \rho = 6/d_e\rho$$

Where d_e is determined using the particle diameters generated by sieving between two sieve sizes:

$$d_e = (d_{max} - d_{min}) / \ln(d_{max}/d_{min})$$

The initial surface area for potential secondary minerals not present in the Tpt is calculated by TOUGHREACT assuming an initial grain radius of 10^{-8} m and an initial (precursor) volume fraction of new forming mineral of 10^{-5}. Using this approach, a mineral's specific surface area is very high when the mineral first precipitates, and then decreases as the mineral abundance increases and the grain size increases. Although arbitrary, this radius is geochemically reasonable and we have found that decreasing this radius by 10x made only minor changes in the results, with the modeled fluid chemistry (being an integration of all the mineral changes) remaining essentially unchanged; the time of each new mineral's first appearance and rate of change with time differed slightly, as would be expected, but by the end of the simulation using a smaller radius the total abundance of each mineral remained essentially the same as that using the larger radius with the exception of a slightly increased kaolinite amount. Therefore, this 10x decrease in initial grain radius did not change the net interpretation of the rock-water interaction.

This simplified mineralogy for the unreacted Tpt wafer (Table 4) was derived from several sources (Delany, 1985, 1985b) and consisted of quartz, cristobalite, plagioclase-ss and microcline. In the simulations the composition of the primary phases (quartz, cristobalite and microcline)

Table 4
Starting mineralogy for idealized Topopah Spring Tuff (Tpt). See text for details on surface area calculation.

Mineral	Volume Fraction	Weight Percent (%)	Specific Surface Area (m²/g)
Quartz (alpha)	0.1507	16.0621	0.4380
Cristobalite (alpha)	0.4449	41.8000	0.4981
Plagioclase-ss	0.1751	18.5000	0.4423
Microcline	0.2294	23.6380	0.4534
Total	1.0001	100.00	

is that of the idealized mineral contained in the thermodynamic database. The composition of the plagioclase-ss is An15, based on the average of 9 EMP-WDS quantitative analyses. Based on the reasoning described in the Discussion section (*4.1*), we included the following minerals contained in the thermodynamic database as potential secondary minerals formed during hydrothermal interaction: montmorillonite-ss, kaolinite, mordeniteB(Ca), mordeniteJ, calcite and magnesite. As mentioned earlier, dachiardite ($Ca_{2.10}K_{0.34}Na_{0.16}$ $[Al_{4.87}Si_{19.15}O_{48}] \bullet 13.9H_2O$ as measured quantitatively post-test) is not in the thermodynamic database that we used, so we elected to include two mordenite minerals from this database as proxies: mordeniteB(Ca) ($Ca_{2.06} [Al_{4.12}Si_{19.88}O_{48}] \bullet 12.4H_2O$), which is calcic, has a Si/Al ratio of around ~5 and is very similar compositionally to our hydrothermally produced dachiardite; and mordeniteJ ($Ca_{1.16}Na_{1.45} [Al_{3.76}Si_{20.24}O_{48}] \bullet$ $13.9H_2O$), which contains both Ca and Na, is compositionally similar to our mordenite run product and is slightly less stable thermodynamically than mordeniteB(Ca) under the conditions of our higher T experiments. The sources for the kinetic data used in the simulations are shown in Table 3.

For subsequent comparison of experiment and model results, we present here modeling results only for those experiments in which we observed identifiable run products: DB9 (250 °C), DB8 (150° - short term) and DB13 (150 °C – long term). The corresponding figures for the two 90 °C experiments are presented in the Appendix (Fig. A2 and A3).

The TOUGHREACT simulation results of the fluid and secondary mineral evolution in the short term run at 250 °C (DB9) are shown in Fig. 3. In these plots the legend entries refer to the names of the primary aqueous species in the model (i.e., the primary variables in the simulation) which reflects the total molality of an element present in multiple different aqueous species and not the concentration of any one individual aqueous species. Recall that the suite of secondary minerals included in the model was based on both preliminary saturation index calculations made using the measured experimental fluid compositions,

wherein all possible mineral phases in the thermodynamic database were considered, as well as the tentative identification of observed secondary minerals found growing on the wafers. For each fluid component we also plot the actual measurements of the experimental fluids sampled during this experiment. These data are tabulated in the Appendix (Tables A2-A8). In the case of pH, plots include both the pH measured in the cooled 25 °C experimental fluid samples, as well as the calculated in-situ 250 °C pH, when the fluid speciation is re-computed at the experiment temperature. This is a single point calculation wherein the 25 °C measured fluid composition is used as the starting point, with pH computed by maintaining a charge balance in the speciation calculations at 25 °C. Because the experimental protocol is designed to mitigate mineral precipitation in the cooled sample (sample filtered, cation split acidified, etc.), precipitation is turned off during this calculation. The code takes the 25 °C total measured fluid composition and recalculates the aqueous speciation and pH at the experimental temperature assuming charge balance. This same process (calculation of in-situ pH, also referred to as a temperature jump) was carried out for the experiments at 150 °C and 90 °C.

The TOUGHREACT simulation results of the fluid and secondary mineral evolution in the short-term run at 150 °C (DB8) are shown in Fig. 4, while the corresponding results for the long-term run at 150 °C (DB13) are shown in Fig. 5.

The TOUGHREACT simulation results of the fluid and secondary mineral evolution in the short term run at 90 °C (DB14) are shown in Appendix Fig. A2, while the corresponding results for the long term run at 90 °C (DB12) are shown in Appendix Fig. A3. In neither of these experiments were we able to identify distinct secondary mineral phases growing on the wafer surfaces.
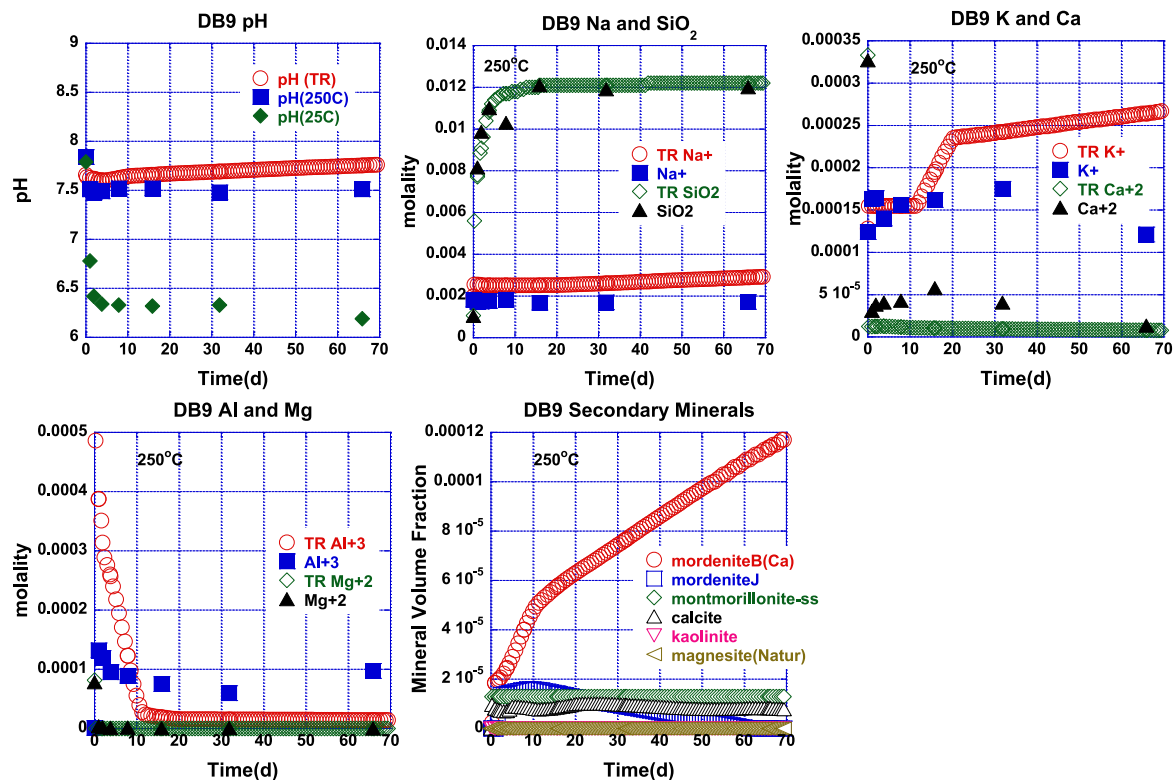

Fig. 3. Simulated TOUGHREACT (TR) evolution of the fluid phase and secondary mineral production in the 66-day run at 250 °C (DB9). In the case of aqueous components, we plot both the TR simulation results (open symbols) and the actual measured fluid composition (closed symbols) for the samples from the physical experiment.
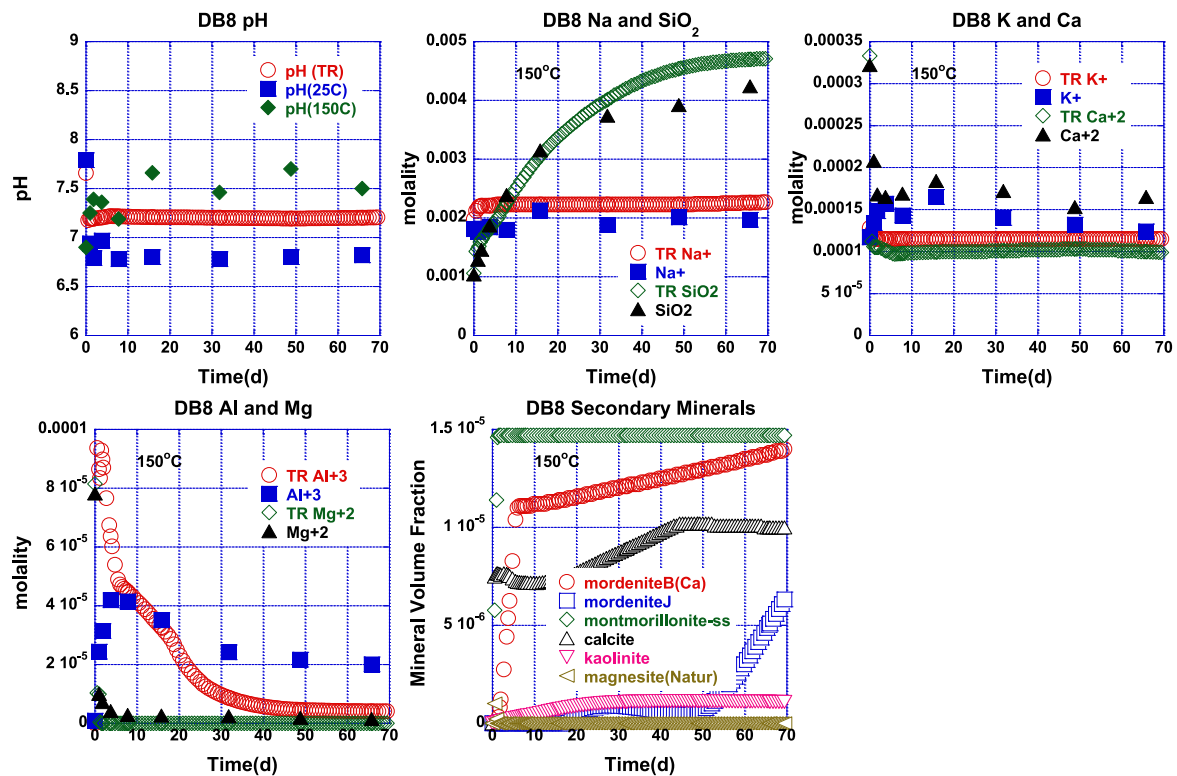
Fig. 4. Simulated TOUGHREACT (TR) evolution of the fluid phase and secondary mineral production in the 66-day run at 150 °C (DB8). In the case of aqueous components, we plot both the TR simulation results (open symbols) and the actual measured fluid composition (closed symbols) for the samples from the physical experiment.
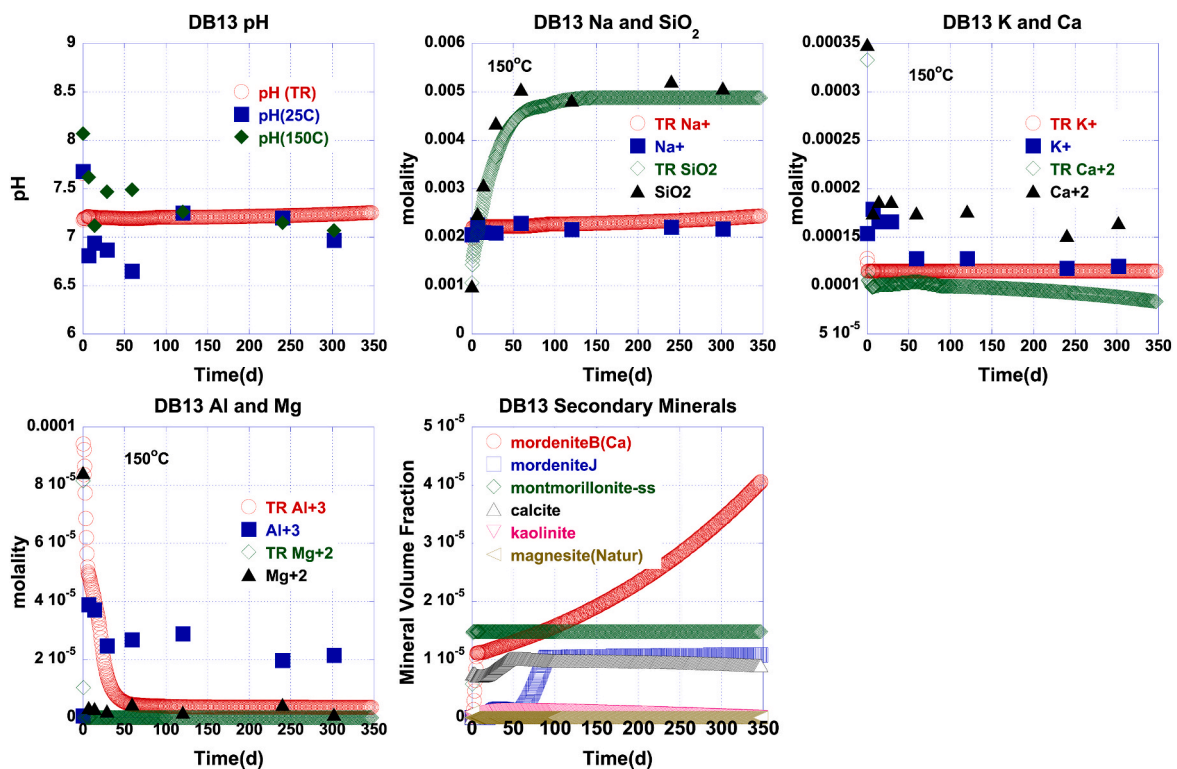

Fig. 5. Simulated TOUGHREACT (TR) evolution of the fluid phase and secondary mineral production in the 303-day run at 150 °C (DB13). In the case of aqueous components, we plot both the TR simulation results (open symbols) and the actual measured fluid composition (closed symbols) for the samples from the physical experiment.

4. Discussion

4.1. Secondary mineral evolution

In addition to the abundant dachiardite and mordenite observed on the DB9 (250 °C) wafer post-test (see Fig. 1a–d), a minor amount of a clay-like phase was seen growing on the surface of the dachiardite crystals (see Fig. 1b), as well as a trace pure-silica phase that formed a perfect sphere (presumed to be cristobalite). Because the clay-like phases were much less abundant and coated the dachiardite, and because mildly alkaline in-situ conditions were generated in the experiment (calculated in-situ pH ~ 7.2, while neutral pH at 250 °C is ~5.5), the clays could have formed as a product of the quench. Conditions near neutral pH tend to favor the formation of phyllosilicates in which Al has a strong preference for six-fold coordination with O, and Si remains in tetrahedral coordination. As pH increases, layer silicates are displaced by tectosilicates (zeolites) in which both Al and Si are in tetrahedral coordination with oxygen (Barrer, 1981). These general arguments suggest that the zeolites dachiardite and mordenite are true run products at 250 °C. At this temperature based on these general observations, the clays could possibly be a quench product. The evolving fluid compositional data provide more insight on this question in the following section, as well as the secondary mineral evolution as a function of time relative to the 150 °C experiments.

At 150 °C in the short-term experiment (DB8) minor clays were present (see Fig. 2a) and Si concentration was still rising (Fig. 4). However, in the longer-term experiment (DB13) no clays were seen, and the Si concentration had risen (Fig. 5) and become quasi-steady state at approximately cristobalite saturation (see following section). This would suggest that at this temperature the clays are ephemeral (in an Ostwald-step-rule sense) at short time, but they are true run products and not a product of the quench. This agrees with the TOUGHREACT simulation results, where in the short term at this temperature (DB8) the dominant run product is montmorillonite-ss (Fig. 4), but in the longer-term experiment (DB13) the zeolite becomes dominant (Fig. 5). The dachiardite run product observed to form (Fig. 2d) in the long-term experiment at 150 °C (DB13) is clearly not a quench product.

The temperature range (150°-250 °C) over which the mordenite group zeolites dachiardite and mordenite formed in these experiments agrees well with that used in the hydrothermal synthesis of these same zeolites in distilled water starting from water-free, compositionally equivalent synthetic glass; the most productive (maximum gain) temperature was found to be about 220 °C (Ghobarkar et al., 2001). No templates or reactive solutions were necessary. These conditions are like those in the experiments reported here.

The agreement between simulation and experiment for the solid phase can only be directly compared at the end of the run when the wafer is recovered but, even so, the comparison is surprisingly good. In the simulations the total abundance of reaction products increases with temperature and the dachiardite proxy (MordeniteB(Ca)) becomes progressively more dominant with increasing temperature and time. The Ca-rich dachiardite predominates over the mixed Na–Ca mordenite (the proxy MordeniteJ in the simulations). This is in agreement with earlier work showing that the alkaline-earth end member zeolites predominate over the alkali end members with increasing temperature (Benning et al., 2000). At 250 °C, in short time and 150 °C in long duration the dachiardite proxy in the simulations is significantly more abundant than the clay. The simulation would suggest that the Ca-rich clay might be a true run product (although relatively minor in abundance and ephemeral), and not simply a quench product, even at the higher temperatures. Given the simplified approach taken by TOUGHREACT to simulate mineral growth and the lack of actual data on growth kinetics, this aspect of the simulation remains speculative. Clearly, more work needs to be done in determining growth kinetics for these clay and zeolite phases (cf. Saldi et al., 2023). Note that the simulations at both 250 °C and 150 °C suggest that calcite should form, yet this phase is not seen on

the recovered wafers. As described below, the composition of the quenched fluid clearly shows that this is simply due to the retrograde solubility of the carbonate minerals: although formed during the run, they redissolve during the cooling of the vessel.

4.2. Fluid chemistry evolution

A key control on silicate secondary mineral formation is the aqueous Si concentration. As can be seen in Fig. 6, the Si concentration in the simulations is being controlled by equilibrium with respect to cristobalite saturation. As noted above (see section 3.1 and Fig. 2c), cristobalite spheres were found to have grown on the reacted wafers in the 250 °C (DB9) and the 150 °C (DB8) experiments. Based on this observation, and the fact that in most experiments at these relatively low temperatures the fluids quickly become supersaturated with respect to quartz and other primary minerals found in the Tpt, we intentionally designed the simulation to suppress the precipitation of all the primary minerals except cristobalite. The primary mineral cristobalite could both dissolve and grow following its kinetic rate law. The other primary minerals could only dissolve following their respective kinetic rate law.

Apart from experiment DB12 (90 °C, long term) which had analytical problems with IC HCO_3^- analyses (and recall that this is a Na–HCO_3 groundwater, whose pH is dominantly controlled by carbonate equilibria), the simulation pH values for all the experiments are within a few tenths of a pH unit of the calculated in-situ experimental pH. The Si results are remarkably close at all 3 temperatures, comparing experiment to simulation. The agreement for the alkalis Na and K is relatively good, Na being somewhat better. The Ca and Mg fluid results show the immediate impact of calcite and magnesite retrograde solubility resulting from heating of the dilute carbonate groundwater to the experimental temperature, in agreement with the production of these secondary minerals in the simulation. The post-quench fluid analyses, which invariably showed both Ca and Mg increasing relative to the last sample acquired at high T&P, explains why we did not find calcite
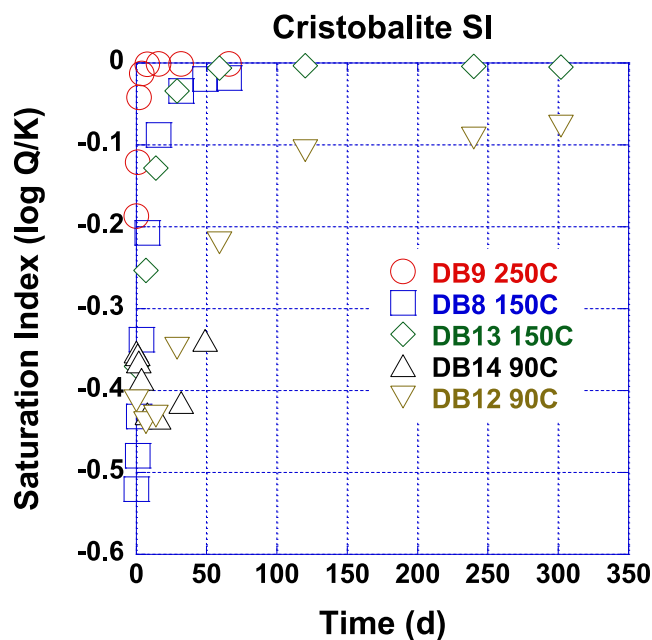

Fig. 6. Saturation Index (log Q/K) for cristobalite in the evolving fluid compositions from the TOUGHREACT simulations at each temperature. For clarity we only plot points corresponding to the experimental sample points in time. SEM evidence shows that pure Si cristobalite spheres did form on the wafers at 250 °C (DB9) and 150 °C (DB8 and DB13), experiments which reached cristobalite saturation, but not in the 90 °C experiments even after nearly 1 year of reaction. See text for details.

growing on the wafer. Any small calcite crystals would have redissolved as the vessel cooled to room temperature. However, following the initial immediate drop in concentration, over the rest of the simulation time the Ca and Mg results compare less well to the experiments (simulation lower than experiment) than for the other metals. As is frequently true, the agreement between model and experiment is worse for Al (cf. Saldi et al., 2023). Initially the model over-predicts Al release, progressively worse as T increases, primarily due to over-predicting the feldspar dissolution rates (White et al., 2017), and then under-predicts Al as time progresses (due to failing to capture the growth kinetics properly). In the physical experiment the Al remains metastably in solution due to various growth inhibition effects, which are not explicitly accounted for in the model.

In TOUGHREACT it is possible to delay the simulated growth of a mineral by requiring a small degree of supersaturation prior to growth (i.e., by requiring that the saturation index, SI, be greater than 0). This is an attempt to account for a delay in mineral growth due to kinetic inhibition. As an exercise using the 250 °C experiment (DB9) as a test case, we attempted to get a better match for fluid Al concentration between experiment and model by both arbitrarily slowing the rate of feldspar (plagioclase-ss and microcline) dissolution by 10 times and by forcing the SI required for zeolite growth to be 0.07. This does decrease the initial Al spike by ~40% and it also increases the Al at longer time (see Fig. A4). However, increasing the SI threshold for zeolite growth also greatly reduces the amount of zeolite produced in the simulation (compare Fig. 3 to Fig. A4). When increasing the SI required for zeolite growth even higher (to 0.2), a closer match in the fluid Al concentration at longer time was obtained, but the match was less good initially (too much Al in the model); also the total amount of zeolite growth decreased even more, eliminating the MorderniteJ (the mordenite proxy) entirely, as only MorderniteB(Ca) (the dachiardite proxy) formed in the simulation (not shown).

This exercise is only included here to illustrate that one may always improve fit of model to experiment by arbitrarily altering a number of input parameters. One of the objectives of this study, however, was to evaluate how well the models perform without resorting to arbitrarily changing thermodynamic and kinetic parameters derived from experimental results reported in the literature from commonly utilized sources. Except for the results shown in Fig. A4 (the fiddling exercise), no changes were made to the thermodynamic and kinetic literature data that were used in any of the other simulations. Nevertheless, the presented TOUGHREACT simulation results are in reasonably good agreement with experimental results.

4.3. Limitations

Use of BET and geometric mineral surface areas in models has been known to frequently yield overestimates of reactivity compared to field measurements. This has been attributed to a variety of factors including: over-estimation of reactive surface area in field settings due to failure to account for heterogeneous flow restrictions or mineral coatings or thickening of leached layers; slowing of rates over time in soils or rocks due to a decrease in surface roughness resulting from weathering; thermodynamic slowing of rates in the field (affinity effect) due to near-equilibrium fluid chemical conditions. Conversely, modeling of laboratory experiments using crushed mineral grains which may contain high energy surface sites and asperities can under-estimate the mineral dissolution rate, if they fail to account for those features (Maher et al., 2009; Moore et al., 2012; White and Brantley, 2003). Recent simulations using literature-obtained BET and geometric specific surface areas provided a reasonable approximation of reactive surface areas in disaggregated lab and field experiments (Beckingham et al., 2016), after accounting for grain size distributions and sample specific phenomena, such as glass dissolution or occlusion of surface area from mineral coatings. Accurate characterization of mineral surfaces and determination of the physico-chemical properties that most affect different

hydraulic parameters (porosity, permeability, hydraulic conductivity, diffusion coefficients, etc.) are fundamental to provide both good estimates of the fluid/mineral interfacial area and better approximations for mineral reactive surface areas.

5. Conclusion

The results of these experiments show that, under mildly hydrothermal conditions, reaction of a densely welded, devitrified high silica rhyolitic tuff with deionized water or a dilute bicarbonate groundwater consistently produced Ca-rich zeolites. One can conclude that similar hydrothermal interactions would result from systems comprised of crystalline rocks in general with similar compositions (alkaline-rich, siliceous granites, etc.). The general conclusion is that in similar rock-dominated systems, it is the rock that largely drives the resulting alteration minerals, when reacted with dilute groundwaters. Production of these particular zeolites (and their alkaline-earth rich compositions) has implications for nuclear waste isolation, geothermal energy production and other processes hosted in compositionally equivalent rock types. For example, the formation of mordenite group zeolites, dominated by the more stable alkaline earth end members at elevated temperatures, is a beneficial result with respect to limiting migration of cationic radioactive metals.

Our results demonstrate the importance of conducting both short term and long-term experiments to evaluate the validity of geochemical simulation models. Short-term experiments allow recovery and observation of solid reaction products that might decrease or even redissolve in longer experiments. Depending on the temperature, at the conclusion of a short-term experiment, the concentrations of many species in the reacted fluid will not be at a kinetic steady state. At the higher temperatures in these experiments the fluid composition does appear to be approaching steady state concentrations for some species (e.g., Si, Al, pH), but at 90 °C reaction rates are so slow that the system is not approaching steady state even after a year of reaction. At lower temperatures even longer time periods might be required (White et al., 2017). In the longer-term steady state might represent equilibrium control by a specific mineral assemblage or simply represent the temporary balance of dissolution of some minerals and growth of others that result in a steady state for any specific fluid component. Running both short- and long-term experiments also allows testing whether in a specific system one can accelerate reaction progress by increasing surface area, i.e., one can produce the same solution composition in short term, high surface area to volume (SA/V) runs as produced in long term, lower SA/V runs. In the case of nuclear waste isolation, one needs to know the solution composition that waste forms (e.g., spent fuel, glass, ceramic, etc.) and canister materials will be exposed to throughout their lifetime to predict their performance using simulations. This calculated fluid composition is the one that would be available to contact, corrode, mobilize (or immobilize) radionuclides contained in the waste form.

Longer term experiments also allow evaluation of the accuracy of simulation results with respect to produced secondary minerals that for the short term might disagree with experiment. Because these simulations use a simplified approach to growth kinetics (and the fact that there is a dearth of data on mineral growth kinetics), any true kinetic inhibition to mineral growth occurring during an experiment delays the appearance of the missing simulation product minerals. Longer experiments would be required to produce them. In these experiments the use of solid wafers of rock provides a means to identify these products more easily. For example, at 150 °C in the short term simulation (DB8), the model predicts slightly higher production of the clay solid solution (montmorillonite-ss) than the zeolite dachiardite proxy (MorderniteB (Ca)), which agrees with post-test observations of the wafer surface. However, after a much longer reaction period, the zeolite minerals were observed in the actual experiment (DB13), again in agreement with the corresponding simulation which showed the zeolite continuing to increase in abundance, whereas the clay was relatively constant over time,

following an initial period of growth, and present at much lower abundance. The experiments confirm that there is, in fact, a kinetic inhibition to the zeolite growth in the short term.

Declaration of competing interest

The authors declare that they have no known competing financial interests or personal relationships that could have appeared to influence the work reported in this paper.

Data availability

Data will be made available on request.

Acknowledgements

Appendix

Table A1

Average J13 water composition based on 11 experimental starting fluid measurements. The J13 water average includes J13 water analyses done spanning the time period over which the subset of reported experiments was conducted.

Sample ID	pH	Na+	K+	Ca++	Mg++	Al+++	Cl-	F-	NO3-	SO4–	HCO3-	SiO2(aq)
		molal	molal	molal	molal	molal	molal	molal	molal	molal	molal	molal
db8-0	7.79	1.81E-03	1.17E-04	3.22E-04	7.82E-05	9.27E-07	1.89E-04	1.21E-04	1.50E-04	1.92E-04	2.93E-03	1.04E-03
db9-0	7.79	1.82E-03	1.24E-04	3.27E-04	7.82E-05	9.64E-07	1.89E-04	1.21E-04	1.50E-04	1.91E-04	1.97E-03	1.04E-03
db10-0	7.86	1.81E-03	1.22E-04	3.27E-04	7.86E-05	2.00E-06	1.83E-04	1.21E-04	1.45E-04	1.83E-04	2.41E-03	1.04E-03
db11-0	7.79	1.74E-03	1.21E-04	3.29E-04	7.74E-05	2.08E-06	1.83E-04	1.16E-04	1.37E-04	1.89E-04	1.90E-03	1.04E-03
db12-0	7.68	2.15E-03	1.28E-04	3.49E-04	8.44E-05	2.22E-07	1.92E-04	1.11E-04	1.39E-04	1.83E-04	1.70E-03	1.10E-03
db13-0	7.68	2.05E-03	1.54E-04	3.49E-04	8.44E-05	6.30E-07	2.00E-04	1.16E-04	1.47E-04	1.94E-04	1.72E-03	9.97E-04
db14-0	7.41	2.18E-03	1.15E-04	3.62E-04	9.47E-05		1.95E-04	1.32E-04	1.44E-04	1.92E-04		1.16E-03
db15-0	7.78	2.13E-03	1.28E-04	3.62E-04	8.23E-05	5.93E-07	1.98E-04	1.16E-04	1.32E-04	1.93E-04		1.09E-03
db20-0	7.65	2.10E-03	1.33E-04	3.10E-04	8.03E-05		2.02E-04	1.16E-04	1.07E-04	2.11E-04	1.88E-03	1.00E-03
db22-0	7.34	2.00E-03	1.20E-04	3.22E-04	8.40E-05		2.02E-04	1.16E-04	1.11E-04	1.87E-04	1.94E-03	1.21E-03
db27-0	7.39	1.97E-03	1.46E-04	3.00E-04	7.49E-05	7.41E-07	2.06E-04	1.11E-04	1.69E-04	1.90E-04	1.74E-03	1.00E-03
J13-average	7.65	1.98E-03	1.28E-04	3.33E-04	8.15E-05	1.11E-06	1.94E-04	1.18E-04	1.39E-04	1.91E-04	2.02E-03	1.07E-03
J13-std_dev	0.19	1.61E-04	1.20E-05	2.05E-05	5.35E-06	7.41E-07	7.62E-06	5.79E-06	1.77E-05	7.50E-06	4.00E-04	6.91E-05

Table A2

Fluid composition for samples from experiment DB14 (90 °C, J13 water).

	ΔT	pH	Na+	K+	Ca++	Mg++	Al+++	Cl-	F-	NO3-	SO4–	HCO3-	SiO2(aq)
	days		molal	molal	molal	molal	molal	molal	molal	molal	molal	molal	molal
db14-0	0.00	7.41	2.18E-03	1.15E-04	3.62E-04	9.47E-05	nm	1.95E-04	1.32E-04	1.44E-04	1.92E-04	2.53E-03	1.16E-03
db14-1	1.00	7.33	2.05E-03	1.28E-04	3.74E-04	7.82E-05	nm	2.02E-04	1.32E-04	1.53E-04	1.93E-04	2.41E-03	9.80E-04
db14-2	1.88	7.3	1.98E-03	1.28E-04	3.62E-04	7.82E-05	nm	1.98E-04	1.26E-04	1.55E-04	1.93E-04	2.34E-03	1.10E-03
db14-4	3.88	7.28	2.09E-03	1.28E-04	3.87E-04	7.41E-05	nm	1.98E-04	1.16E-04	1.55E-04	1.92E-04	2.53E-03	1.37E-03
db14-8	7.88	7.18	2.09E-03	1.28E-04	3.74E-04	7.00E-05	nm	2.06E-04	1.26E-04	1.60E-04	1.97E-04	2.52E-03	1.25E-03
db14-17	16.88	7.19	2.09E-03	1.28E-04	3.62E-04	7.00E-05	nm	2.00E-04	1.26E-04		1.94E-04	2.67E-03	1.35E-03
db14-32	31.88	7.11	2.18E-03	1.41E-04	3.72E-04	7.20E-05	nm	2.29E-04	1.42E-04	1.57E-04	1.98E-04	2.64E-03	1.24E-03
db14-49	48.88	7.07	2.22E-03	1.41E-04	3.69E-04	7.41E-05	nm	1.95E-04	1.16E-04	1.48E-04	1.87E-04	2.83E-03	1.23E-03

nm = not measured.

Table A3

Fluid composition for samples from experiment DB12 (90 °C, J13 water).

Sample	ΔT	pH	Na+	K+	Ca++	Mg++	Al+++	Cl-	F-	NO3-	SO4–	HCO3-	SiO2(aq)
	days		molal	molal	molal	molal	molal	molal	molal	molal	molal	molal	molal
db12-0	0	7.68	2.15E-03	1.28E-04	3.49E-04	8.44E-05	2.22E-07	1.92E-04	1.11E-04	1.39E-04	1.83E-04	1.71E-03	1.10E-03
db12-8	6.96	7.39	2.02E-03	1.54E-04	3.62E-04	6.59E-05	2.08E-06	2.00E-04	1.26E-04	1.48E-04	2.05E-04	2.12E-03	1.12E-03
db12-15	13.96	7.5	2.22E-03	1.66E-04	3.49E-04	6.58E-05	2.45E-06	2.09E-04	1.32E-04	1.45E-04	2.03E-04	2.46E-03	1.12E-03
db12-30	28.96	7.25	2.03E-03	1.66E-04	3.74E-04	6.59E-05	2.82E-06	2.00E-04	1.32E-04	1.58E-04	2.00E-04	2.41E-03	1.18E-03
db12-60	58.96	7.14	2.28E-03	1.41E-04	3.87E-04	6.79E-05	1.71E-06	1.98E-04	1.26E-04	1.55E-04	1.93E-04	1.92E-03	1.46E-03
db12-121	120.13	7.26	2.20E-03	1.41E-04	3.44E-04	5.35E-05	1.34E-06	2.03E-04	1.16E-04	1.36E-04	1.94E-04	2.10E-03	1.47E-03
db12-241	239.96	7.12	2.02E-03	1.54E-04	3.35E-04	5.60E-05	7.04E-06	1.95E-04	1.05E-04	1.69E-04	1.93E-04	2.36E-03	1.63E-03
db12-303	301.96	7.19	2.04E-03	1.69E-04	3.47E-04	5.06E-05	7.79E-06	2.12E-04	1.16E-04	1.39E-04	2.17E-04	2.03E-03	1.69E-03
db12-304	304.96	6.57	1.91E-03	1.28E-04	3.47E-04	5.39E-05	7.42E-06	2.09E-04	1.16E-04	1.47E-04	2.15E-04	2.00E-03	1.68E-03

Table A4
Fluid composition for samples from experiment DB8 (150 °C, J13 water).

Sample	ΔT	pH	Na+	K+	Ca++	Mg++	Al+++	Cl-	F-	NO3-	SO4–	HCO3-	SiO2(aq)
	days		molal	molal	molal	molal	molal	molal	molal	molal	molal	molal	molal
db8-0	0	7.79	1.81E-03	1.17E-04	3.22E-04	7.82E-05	9.27E-07	1.89E-04	1.21E-04	1.47E-04	1.92E-04	2.93E-03	1.04E-03
db8-1	0.96	6.94	1.76E-03	1.34E-04	2.08E-04	1.00E-05	2.44E-05	1.98E-04	1.21E-04	1.40E-04	1.92E-04	1.74E-03	1.29E-03
db8-2	1.81	6.79	1.82E-03	1.48E-04	1.68E-04	7.20E-06	3.14E-05	1.95E-04	1.21E-04	1.40E-04	1.91E-04	1.58E-03	1.46E-03
db8-4	3.77	6.97	1.84E-03	1.57E-04	1.65E-04	4.20E-06	4.19E-05	1.86E-04	1.16E-04	1.45E-04	1.86E-04	1.62E-03	1.87E-03
db8-8	7.81	6.78	1.80E-03	1.43E-04	1.69E-04	2.84E-06	4.15E-05	2.82E-04	1.16E-04	1.37E-04	1.84E-04	1.63E-03	2.39E-03
db8-16	15.81	6.8	2.13E-03	1.65E-04	1.84E-04	2.63E-06	3.51E-05	2.17E-04	1.37E-04	1.40E-04	1.79E-04	1.57E-03	3.15E-03
db8-32	31.81	6.78	1.88E-03	1.40E-04	1.72E-04	2.43E-06	2.42E-05	1.89E-04	1.21E-04	1.39E-04	1.75E-04	1.51E-03	3.74E-03
db8-49	48.81	6.8	2.01E-03	1.32E-04	1.53E-04	1.89E-06	2.17E-05	1.83E-04	1.05E-04	1.44E-04	1.76E-04	1.33E-03	3.92E-03
db8-66	65.81	6.82	1.97E-03	1.24E-04	1.65E-04	1.44E-06	2.01E-05	1.92E-04	1.11E-04	1.36E-04	1.78E-04	1.54E-03	4.24E-03

Table A5
Fluid composition for samples from experiment DB13 (150 °C, J13 water).

Sample	ΔT	pH	Na+	K+	Ca++	Mg++	Al+++	Cl-	F-	NO3-	SO4–	HCO3-	SiO2(aq)
	days		molal	molal	molal	molal	molal	molal	molal	molal	molal	molal	molal
db13-0	0.00	7.68	2.05E-03	1.54E-04	3.49E-04	8.44E-05	6.30E-07	2.00E-04	1.16E-04	1.47E-04	1.94E-04	1.72E-03	9.97E-04
db13-8	6.96	6.81	2.26E-03	1.79E-04	1.75E-04	3.50E-06	3.89E-05	2.03E-04	1.32E-04	1.61E-04	2.04E-04	1.75E-03	2.49E-03
db13-15	14.00	6.94	2.10E-03	1.66E-04	1.87E-04	3.17E-06	3.71E-05	2.15E-04	1.32E-04	1.63E-04	2.01E-04	2.18E-03	3.08E-03
db13-30	29.00	6.87	2.09E-03	1.66E-04	1.87E-04	2.31E-06	2.47E-05	2.06E-04	1.32E-04	1.60E-04	2.01E-04	1.66E-03	4.36E-03
db13-60	58.96	6.65	2.29E-03	1.28E-04	1.75E-04	4.73E-06	2.68E-05	1.98E-04	1.26E-04	1.50E-04	1.92E-04	1.80E-03	5.06E-03
db13-121	120.13	7.25	2.16E-03	1.28E-04	1.77E-04	1.85E-06	2.89E-05	2.06E-04	1.21E-04	1.73E-04	1.95E-04	1.94E-03	4.83E-03
db13-241	240.00	7.2	2.21E-03	1.18E-04	1.52E-04	4.53E-06	1.97E-05	2.03E-04	1.05E-04	1.63E-04	1.82E-04	2.18E-03	5.22E-03
db13-303	302.00	6.97	2.17E-03	1.20E-04	1.65E-04	1.19E-06	2.15E-05	2.17E-04	1.16E-04	1.55E-04	2.16E-04	2.20E-03	5.08E-03
db13-304	304.00	6.14	2.21E-03	1.05E-04	3.72E-04	3.79E-06	1.71E-05	2.12E-04	1.16E-04	1.47E-04	2.16E-04	1.94E-03	5.04E-03

Table A6
Fluid composition for samples from experiment DB9 (250 °C, J13 water).

Sample	ΔT	pH	Na+	K+	Ca++	Mg++	Al+++	Cl-	F-	NO3-	SO4–	HCO3-	SiO2(aq)
	days		molal	molal	molal	molal	molal	molal	molal	molal	molal	molal	molal
db9-0	0.00	7.79	1.82E-03	1.24E-04	3.27E-04	7.82E-05	9.64E-07	1.89E-04	1.21E-04	1.50E-04	1.91E-04	1.97E-03	1.04E-03
db9-1	1.00	6.78	1.72E-03	1.63E-04	3.10E-05	3.79E-06	1.32E-04	1.95E-04	1.32E-04	1.53E-04	1.92E-04	1.15E-03	8.16E-03
db9-2	1.90	6.42	1.73E-03	1.64E-04	3.82E-05	2.18E-06	1.19E-04	1.98E-04	1.32E-04	1.53E-04	1.93E-04	1.27E-03	9.87E-03
db9-4	3.81	6.34	1.76E-03	1.40E-04	4.07E-05	8.65E-07	9.53E-05	1.98E-04	1.32E-04	1.53E-04	1.93E-04	1.17E-03	1.10E-02
db9-8	7.85	6.33	1.82E-03	1.56E-04	4.27E-05	1.32E-06	8.90E-05	1.98E-04	1.37E-04	1.52E-04	1.90E-04	1.32E-03	1.03E-02
db9-16	15.85	6.32	1.67E-03	1.62E-04	5.77E-05	3.71E-07	7.49E-05	1.89E-04	1.42E-04	1.49E-04	1.81E-04	9.30E-04	1.21E-02
db9-32	31.85	6.33	1.69E-03	1.75E-04	4.05E-05	7.00E-07	5.97E-05	1.95E-04	1.32E-04	1.52E-04	1.92E-04	1.31E-03	1.19E-02
db9-66	65.85	6.19	1.71E-03	1.21E-04	1.35E-05	2.47E-07	9.72E-05	1.95E-04	1.32E-04	1.52E-04	1.92E-04	7.00E-04	1.20E-02

Table A7
Fluid composition for samples from experiment DB17 (90 °C, MQ water).

Sample	ΔT	pH	Na+	K+	Ca++	Mg++	Al+++	Cl-	F-	NO3-	SO4–	HCO3-	SiO2(aq)
	days		molal	molal	molal	molal	molal	molal	molal	molal	molal	molal	molal
db17-0	0	4.97	6.09E-05	3.84E-05	1.37E-05	1.36E-05	1.33E-06	5.64E-05	nm	1.11E-04		2.00E-05	1.75E-06
db17-1	1	6.23	1.00E-04	2.56E-05	1.15E-05	1.50E-05	2.63E-06	4.23E-05	nm	1.20E-04		4.00E-05	5.38E-05
db17-2	1.88	6.33	1.00E-04	3.84E-05	1.37E-05	1.44E-05	3.41E-06	4.51E-05	nm	1.21E-04		6.00E-05	6.45E-05
db17-4	3.88	6.18	1.04E-04	2.56E-05	1.25E-05	1.65E-05	2.26E-06	3.10E-05	nm	4.60E-05	4.16E-05	7.00E-05	8.69E-05
db17-8	7.88	6.55	1.24E-04	3.84E-05	1.17E-05	1.44E-05	5.00E-06	3.67E-05	nm	6.95E-05	4.16E-05	4.00E-05	1.22E-04
db17-16	15.88	6.29	6.48E-05	2.30E-05		1.38E-05	6.08E-06	2.82E-05	nm			1.90E-04	1.95E-04
db17-32	31.85		1.61E-04	5.12E-05		2.26E-05	1.35E-05	3.95E-05	nm			6.00E-05	3.39E-04
db17-49	48.88	6.93	8.44E-05		9.48E-06	3.21E-06	1.78E-05	4.23E-05	nm			8.00E-05	4.56E-04
db17-64	63.88	6.57	1.11E-04	5.12E-05	6.49E-06	4.12E-06	1.15E-05	2.82E-05	nm			2.50E-04	5.70E-04

Table A8
Fluid composition for samples from experiment DB16 (150 °C, MQ water).

| Sample	ΔT	pH	Na+	K+	Ca++	Mg++	Al+++	Cl-	F-	NO3-	SO4--	HCO3-	SiO2(aq)
	days		molal	molal	molal	molal	molal	molal	molal	molal	molal	molal	molal
db16-0	0	4.8	2.07E-04	2.56E-05	2.12E-05	1.38E-05	1.59E-06	1.13E-05	nm	3.08E-04		4.00E-05	2.46E-06
db16-1	1	6.4	2.07E-04	5.12E-05	1.75E-05	1.58E-05	7.56E-06	2.26E-05	nm	2.34E-04		1.30E-04	1.03E-04
db16-2	1.88	6.6	2.46E-04	6.39E-05	1.50E-05	1.46E-05	2.47E-05	2.26E-05	nm	2.48E-04		1.70E-04	3.12E-04
db16-4	3.88	6.5	3.11E-04	7.67E-05	1.37E-05	1.81E-05	4.26E-05	1.13E-05	nm	3.00E-04		2.80E-04	0.001095
db16-8	7.88	6.6	4.66E-04	7.67E-05	1.37E-05	1.63E-05	4.08E-05		nm	3.79E-04		3.70E-04	0.001834
db16-16	15.88	6.7	4.13E-04	6.78E-05	4.99E-06	1.58E-05	4.63E-05		nm	8.79E-05		6.40E-04	0.003312
db16-32	31.85	7.1	6.44E-04	7.04E-05	3.99E-06	2.26E-05	4.26E-05	3.10E-05	nm	1.02E-04	3.12E-05	6.70E-04	0.004203
db16-49	48.88	7.5	6.05E-04		8.99E-06	8.64E-06	5.19E-05	3.95E-05	nm	1.61E-06		6.50E-04	0.004702
db16-64	63.88	7.4	6.09E-04		5.49E-06	4.53E-06	4.82E-05	3.10E-05	nm	1.37E-05		5.90E-04	0.004808
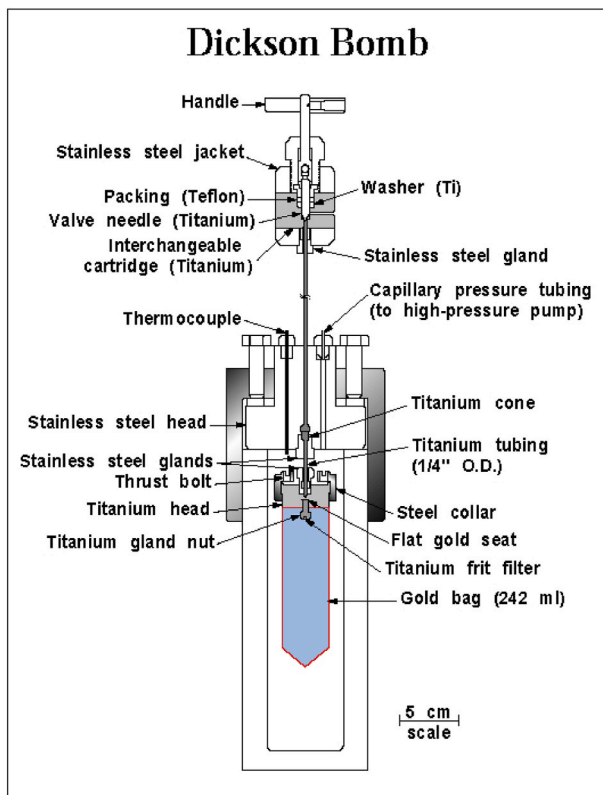
Fig. A1. Schematic diagram of the flexible Au bag reactor system.
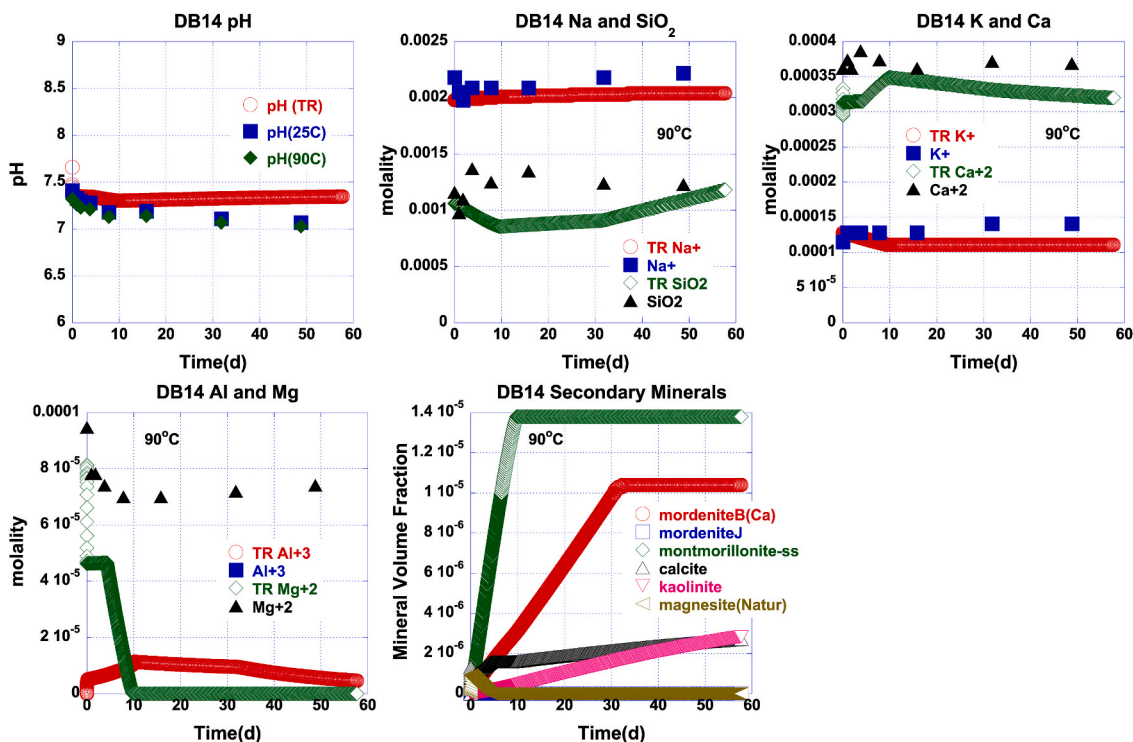
Fig. A2. Simulated TOUGHREACT (TR) evolution of the aqueous phase and secondary mineral production in the 50-day run at 90 °C (DB14), that used deionized water. In the case of fluid components, we plot both the TR simulation results (open symbols) and the actual measured fluid composition (closed symbols) for the samples from the physical experiment. Note that in this experiment the Al concentration was at or below detection limit and is not plotted.
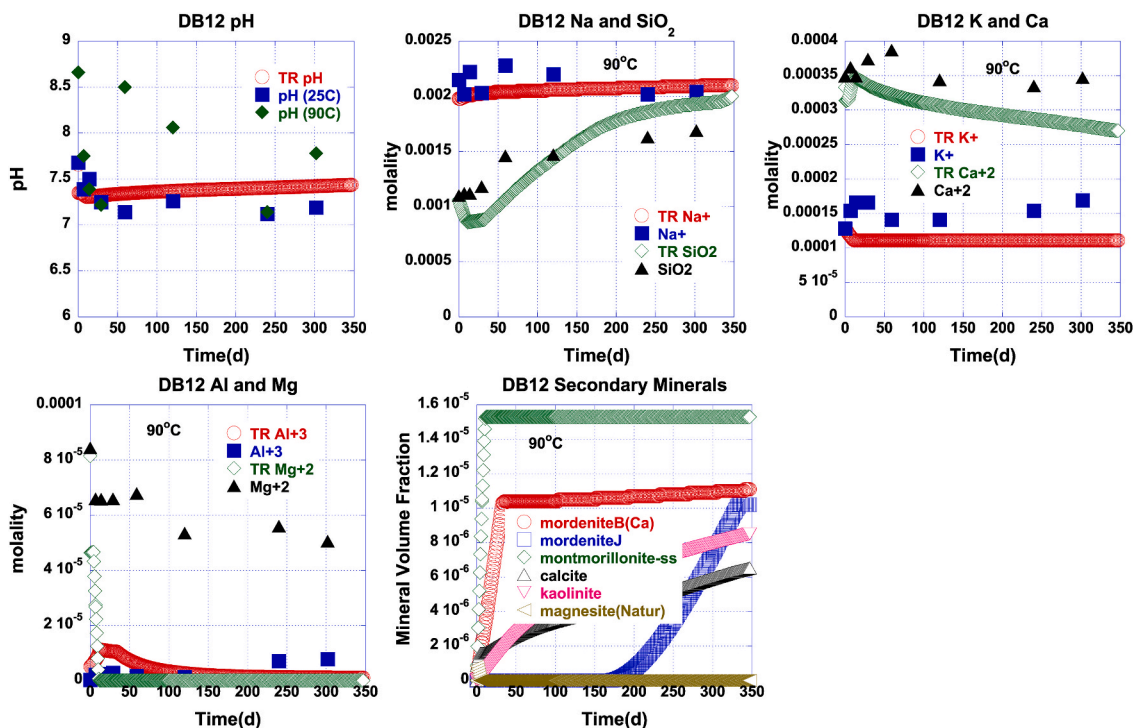

Fig. A3. Simulated TOUGHREACT (TR) evolution of the fluid phase and secondary mineral production in the 302-day run at 90 °C (DB12), that used deionized water. In the case of aqueous components, we plot both the TR simulation results (open symbols) and the actual measured fluid composition (closed symbols) for the samples from the physical experiment. Note that there were analytical problems with the IC measurement of HCO3- during this experiment, adversely impacting the in-situ pH calculation. See text for details.
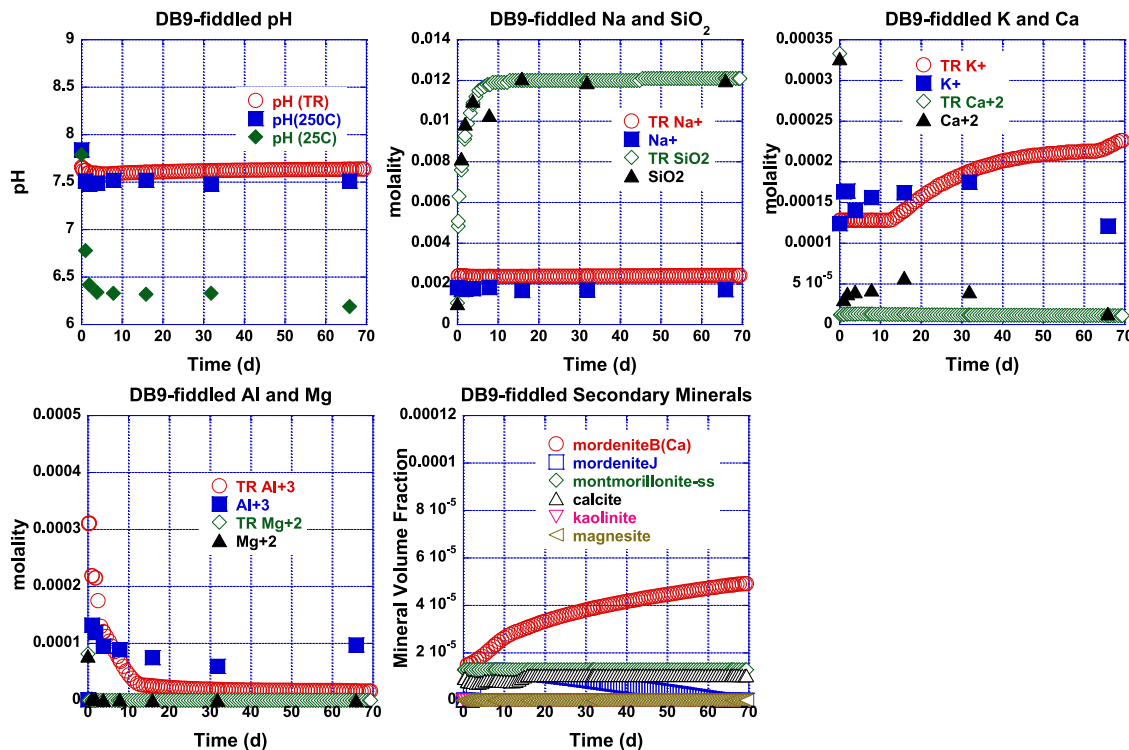
Fig. A4. An attempt to improve Al fit (experiment to model) in the 250 °C experiment (DB9) by slowing feldspar dissolution and delaying zeolite mineral growth. Simulated TOUGHREACT (TR) evolution of the aqueous phase and secondary mineral production are shown. These can be compared to those shown in Fig. 3. Details are in the text.

References

Alberti, A., 1975. Sodium-rich dachiardite from alpe-di-siusi, Italy. Contrib. Mineral. Petrol. 49 (1), 63–66. https://doi.org/10.1007/bf00371079.

Aradottir, E.S.P., Sonnenthal, E.L., Jonsson, H., 2012. Development and evaluation of a thermodynamic dataset for phases of interest in CO2 mineral sequestration in basaltic rocks. Chem. Geol. 304, 26–38. https://doi.org/10.1016/j.chemgeo.2012.01.031.

Bargar, K.E., Erd, R.C., Keith, T.E.C., Beeson, M.H., 1987. Dachiardite from yellowstone-national-park, Wyoming. Can. Mineral. 25, 475–483.

Bargar, K.E.a., Beeson, M.H., 1981. Hydrothermal alteration in research drill hole Y-2, lower Geyser Basin, Yellowstone-National-Park, Wyoming. Am. Mineral. 66 (5–6), 473–490.

Barrer, R.M., 1981. Zeolites and their synthesis. Zeolites 1 (3), 130–140. https://doi.org/10.1016/s0144-2449(81)80001-2.

Beckingham, L.E., Mitnick, E.H., Steefel, C.I., Zhang, S., Voltolini, M., Swift, A.M., Yang, L., Cole, D.R., Sheets, J.M., Ajo-Franklin, J.B., DePaolo, D.J., Mito, S., Xue, Z. Q., 2016. Evaluation of mineral reactive surface area estimates for prediction of reactivity of a multi-mineral sediment. Geochem. Cosmochim. Acta 188, 310–329. https://doi.org/10.1016/j.gca.2016.05.040.

Benning, L.G., Wilkin, R.T., Barnes, H.L., 2000. Solubility and stability of zeolites in aqueous solution: II. Calcic clinoptilolite and mordenite. Am. Mineral. 85 (3–4), 495–508. https://doi.org/10.2138/am-2000-0411.

Bi, Y.Z.W., Prentice, D.P., Ryan, J.V., Ellison, K., Bauchy, M., Sant, G., 2020. zeo19: a thermodynamic database for assessing zeolite stability during the corrosion of nuclear waste immobilization glasses. npj Materials Degradation 4 (1). https://doi.org/10.1038/s41529-019-0106-1.2.

Bish, D.L., Caporuscio, F.A., Copp, J.F., Crowe, B.M., Purson, J.D., Smyth, J.R., Warren, R.S., 1981. Preliminary Stratigraphic and Petrologic Characterization of Core Samples from USW-G1, Yucca Mountain, Nevada, LA-8840-MS. Los Alamos National Laboratory.

Blanc, P., Lassin, A., Piantone, P., Azaroual, M., Jacquemet, N., Fabbri, A., Gaucher, E.C., 2012. Thermoddem: a geochemical database focused on low temperature water/rock interactions and waste materials. Appl. Geochem. 27 (10), 2107–2116. https://doi.org/10.1016/j.apgeochem.2012.06.002.

Blum, A.E., Stillings, L.L., 1995. Feldspar dissolution kinetics. In: White, A.F., Brantley, S. L. (Eds.), Chemical Weathering Rates of Silicate Minerals. MIneralogical Society of America, Washington, D. C., pp. 291–351

Bonardi, M., 1979. Composition of type dachiardite from Elba - re-examination. Mineral. Mag. 43 (328), 548–549. https://doi.org/10.1180/minmag.1979.043.328.19.

Bonardi, M., Roberts, A.C., Sabina, A.P., Chao, G.Y., 1981. Sodium-rich dachiardite from the francon quarry, montreal island, quebec. Can. Mineral. 19, 285–289.

Christiansen, R.L., Lipman, P.W., Carr, W.J., Byers, F.M., Orkild, P.P., Sargent, K.A., 1977. Timber Mountain - oasis Valley caldera complex of southern Nevada. Geol. Soc. Am. Bull. 88 (7), 943–959. https://doi.org/10.1130/0016-7606, 1977)88<943: Tmvcco>2.0.Co;2.

Delany, J.M., 1985. Reaction of Topopah Spring Tuff with J-13 Water: A Geochemical Modeling Approach Using the Eq3/6 Reaction Path Code, UCRL-53631. Lawrence Livermore National Laboratory.

Gellens, L.R., Price, G.D., Smith, J.V., 1982. The structural relation between svetlozarite and dachiardite. Mineral. Mag. 45, 157–161. https://doi.org/10.1180/minmag.1982.045.337.18.

Ghobarkar, H., Schaf, O., Guth, U., 2001. The use of the high pressure hydrothermal method for tailored synthesis of zeolites without structure directing agents. Instance: synthesis of natural zeolites with 5-1 building units. High Pres. Res. 20 (1–6), 45–53. https://doi.org/10.1080/08957950108206151.

Knauss, K.G., Beiriger, W.J., Peifer, D.W., 1985a. Hydrothermal Interaction of Crushed Topopah Springs Tuff with J13 Water at 90°C, 150°C and 250°C Using the Dickson-type Gold-Bag Rocking Autoclave, UCRL-53630. Lawrence Livermore National Laboratory.

Knauss, K.G., Beiriger, W.J., Peifer, D.W., Piwinski, A.J., 1985b. Hydrothermal Interaction of Solid Wafers of Topopah Spring Tuff with J13 Water and Distilled Water at 90°C, 150°C and 250°C Using the Dickson-type Gold-Bag Rocking Autoclave, UCRL-53645. Lawrence Livermore National Laboratory.

Knauss, K.G., Beiringer, W.J., Peifer, D.W., 1987. Hydrothermal Interaction of Solid Wafers of Topopah Spring Tuff with J-13 Water at 90 and 150C Using Dickson-type Gold Bag Rocking Autoclaves: Long-Term experiments., UCRL-53722. Lawrence Livermore National Laboratory.

Lasaga, A.C., 1984. Chemical kinetics of water-rock interactions. J. Geophys. Res. 89 (B6), 4009–4025.

Lichtner, P.C., 2016. Kinetic rate laws invariant to scaling the mineral formula unit. Am. J. Sci. 316 (5), 437–469. https://doi.org/10.2475/05.2016.02.

Maher, K., Steefel, C.I., White, A.F., Stonestrom, D.A., 2009. The role of reaction affinity and secondary minerals in regulating chemical weathering rates at the Santa Cruz Soil Chronosequence, California. Geochem. Cosmochim. Acta 73 (10), 2804–2831. https://doi.org/10.1016/j.gca.2009.01.030.

Marieni, C., Voigt, M.J., Oelkers, E.H., 2021. Experimental study of epidote dissolution rates from pH 2 to 11 and temperatures from 25 to 200 degrees C. Geochem. Cosmochim. Acta 294, 70–88. https://doi.org/10.1016/j.gca.2020.11.015.

Moore, J., Lichtner, P.C., White, A.F., Brantley, S.L., 2012. Using a reactive transport model to elucidate differences between laboratory and field dissolution rates in regolith. Geochem. Cosmochim. Acta 93, 235–261. https://doi.org/10.1016/j.gca.2012.03.021.

Nishido, H., Otsuka, R., 1981. Chemical composition and physical properties of dachiardite group zeolites. Mineral. J. 10 (8), 371–384.

Oelkers, E.H., Schott, J., Devidal, J.-L., 1994. The effect of aluminum, pH, and chemical affinity on the rates of aluminosilicate dissolution reactions. Geochem. Cosmochim. Acta 58 (9), 2011–2024.

Oelkers, E.H., Schott, J., Gauthier, J.M., Herrero-Roncal, T., 2008. An experimental study of the dissolution mechanism and rates of muscovite. Geochem. Cosmochim. Acta 72 (20), 4948–4961. https://doi.org/10.1016/j.gca.2008.01.040.

Oelkers, E.H., Gislason, S.R., 2001. The mechanism, rates and consequences of basaltic glass dissolution: I. An experimental study of the dissolution rates of basaltic glass as a function of aqueous Al, Si and oxalic acid concentration at 25 degrees C and pH=3 and 11. Geochem. Cosmochim. Acta 65 (21), 3671–3681. https://doi.org/10.1016/s0016-7037(01)00664-0.

Ogorodova, L.P., Mel`chakova, L.V., Kiseleva, I.A., 2007. A study of dachiardite, a natural zeolite of the mordenite group. Russ. J. Phys. Chem. 81 (11), 1748–1750.

Palandri, J.L., Kharaka, Y.K., 2004. A Compilation of Rate Parameters of Water-Mineral Interaction Kinetics for Application to Geochemical Modeling. USGS Open File Report, 2004-1068.

Passaglia, E., 1970. The crystal chemistry of chabazites. Am. Mineral. 55, 1278–1301.

Rutqvist, J., Tsang, C.F., 2012. Multiphysics processes in partially saturated fractured rock: experiments and models from yucca mountain. Rev. Geophys. 50 https://doi.org/10.1029/2012rg000391.Rg3006.

Saldi, G.D., Knauss, K.G., Spycher, N., Oelkers, E.H., Jones, A.P., 2023. A combined experimental and modelling study of granite hydrothermal alteration. Geothermics 108, 102633.

Savage, D., Cave, M.R., Haigh, D., Milodowski, A.E., Young, M.E., 1993. The reaction-kinetics of laumontite under hydrothermal conditions. Eur. J. Mineral 5 (3), 523–535.

Seyfried, W.E., Gordon, P.C., Dickson, F.W., 1979. A new reaction cell for hydrothermal solution equipment. Am. Mineral. 64, 646–649.

Sheldrick, G.M., 2008. A short history of SHELX. Acta Crystallographica a-Foundation and Advances 64, 112–122. https://doi.org/10.1107/s0108767307043930.

Testor, J.W., Worley, W.G., Robinson, B.A., Grigsby, C.O., Feerer, J.L., 1994. Correlating quartz dissolution kinetics in pure water from 25 to 625°C. Geochem. Cosmochim. Acta 58, 2407–2420.

White, A.F., Schulz, M.S., Lawrence, C.R., Vivit, D.V., Stonestrom, D.A., 2017. Long-term flow-through column experiments and their relevance to natural granitoid weathering rates. Geochem. Cosmochim. Acta 202, 190–214. https://doi.org/10.1016/j.gca.2016.11.042.

White, A.F.a., Brantley, S.L., 2003. The effect of time on the weathering of silicate minerals: why do weathering rates differ in the laboratory and field? Chem. Geol. 202 (3–4), 479–506. https://doi.org/10.1016/j.chemgeo.2003.03.001.

Wise, W.S., Tschernik, R.W., 1978. Dachiardite-bearing zeolite assemblages in the pacific northwest. In: Sand, L.B.a.M., F.A (Eds.), Natural Zeolites: Occurrences, Properties. Pergammon, Oxford, England, pp. 105–111.

Xu, T., Sonnenthal, E.L., Spycher, N., Pruess, K., 2006. TOUGHREACT: a simulation program for non-isothermal multiphase reactive geochemical transport in variably saturated geologic media. Comput. Geosci. 32, 145–165.

Xu, T.F., Spycher, N., Sonnenthal, E., Zhang, G.X., Zheng, L.E., Pruess, K., 2011. TOUGHREACT Version 2.0: a simulator for subsurface reactive transport under non-isothermal multiphase flow conditions. Comput. Geosci. 37 (6), 763–774. https://doi.org/10.1016/j.cageo.2010.10.007.